Journal of Magnetism and Magnetic Materials 655 (2026) 174343

Contents lists available at ScienceDirect

Journal of Magnetism and Magnetic Materials

journal homepage: www.elsevier.com/locate/jmmm

Stepwise seed-mediated growth of multiphase spinel@Wüstite Core–Shell nanoparticles with exchange-coupled magnetic properties☆

Kevin Sartori [a,b], Fadi Choueikani [b], Simon Hettler [c], Raul Arenal [d,e,f], Benoit P. Pichon [a,g,*]

[a] Université de Strasbourg, CNRS, Institut de Physique et Chimie des Matériaux de Strasbourg, UMR 7504, F-67000 Strasbourg, France
[b] Synchrotron SOLEIL, L'Orme des Merisiers, Départementale 128, 91190 Saint-Aubin, France
[c] Laboratory for Electron Microscopy (LEM), Karlsruhe Institute for Technology, Engesserstr. 7, 76131 Karlsruhe, Germany
[d] Instituto de Nanociencia y Materiales de Aragon (INMA), CSIC-Universidad de Zaragoza, Calle Pedro Cerbuna 12, 50009 Zaragoza, Spain
[e] Laboratorio de Microscopías Avanzadas (LMA), Universidad de Zaragoza, Calle Mariano Esquillor, 50018 Zaragoza, Spain
[f] ARAID Foundation, Avenida de Ranillas, 50018 Zaragoza, Spain
[g] Institut Universitaire de France, 1 rue Descartes, 75231 Paris Cedex 05, France

ARTICLE INFO

Keywords:
Nanoparticles
Multi-step synthesis
Exchange-coupling
Interface
Anisotropy

ABSTRACT

A series of exchange-coupled magnetic nanoparticles featuring multiple magnetic phases arranged in a core-shell architecture was synthesized through a three-step seed-mediated growth process. Iron, cobalt, and nickel precursors were sequentially thermally decomposed in high-boiling-point solvents (approximately 300 °C), enabling the successive growth of CoO and NiO shells on Fe_3O_4 nanoparticle's cores. The structural and chemical characteristics of these nanoparticles were thoroughly investigated using a combination of advanced analytical techniques, including scanning transmission electron microscopy (STEM) in high-angle annular dark-field imaging mode (HAADF), electron energy-loss spectroscopy STEM (EELS-STEM), and X-ray magnetic circular dichroism (XMCD). After each thermal decomposition step, the nanoparticle size progressively increased, accompanied by noticeable changes in morphology, indicating significant surface reconstruction. Furthermore, the chemical structure proved to be more complex than initially anticipated. The high synthesis temperature promoted cation interdiffusion at the interfaces as well as partial dissolution–recrystallization processes at the nanoparticle surface. An intermixed Co/Ni shell, composed of a combination of wüstite and spinel phases, was found to influence the magnetic properties of the nanoparticles through exchange bias coupling. This effect is directly correlated with the relative proportions of Co and Ni cations incorporated within the shell.

1. Introduction

Magnetic nanoparticles that combine sizable magnetic anisotropy with a composition drawn exclusively from earth-abundant elements are increasingly viewed as key building blocks for cost-effective, sustainable technologies ranging from heat-assisted catalysis and magnetic hyperthermia to high-density data storage [1]. However, transition metal oxide nanoparticles usually undergo a transition to the superparamagnetic behavior at room temperature, i.e. low or nonexistent capability to store magnetic energy [2,3]. Therefore, strategies to compensate size effects in order to produce nanoparticles with enhanced magnetic anisotropy, i.e. blocked magnetic moments at room temperature have to be developed. A promising way is the combination of such soft magnetic nanomaterials with a harder magnetic phase in order to design core-shell structure in a single nanoparticle [4]. Such bi-magnetic structures induce exchange coupling at the interface through the pinning of soft spins by hard spins at the core-shell interface. It results in an additional unidirectional anisotropy after cooling down under a magnetic field below the Néel temperature (T_N) of the hard antiferromagnetic phase. Therefore, exchange coupling undergoes an extra energy barrier for the reversal of soft spins when applying a magnetic field in the opposite direction. It results in a larger hysteresis loop, which is shifted to the opposite direction of the cooling field, testifying of the exchange bias field (H_E).

Design of core-shell nanoparticles has been widely investigated in order to favor large interfaces between soft and hard phases for efficient exchange coupling. Ferrimagnetic (FiM) ferrite MFe_2O_4 and antiferromagnetic (AFM) MO are efficient materials because their magnetic

☆ This article is part of a Special issue entitled: 'Magnetic Nanoparticles (ICFPM 2025)' published in Journal of Magnetism and Magnetic Materials.

* Corresponding author at: Université de Strasbourg, CNRS, Institut de Physique et Chimie des Matériaux de Strasbourg, UMR 7504, F-67000 Strasbourg, France.
E-mail address: Benoit.Pichon@unistra.fr (B.P. Pichon).

https://doi.org/10.1016/j.jmmm.2026.174343
Received 31 March 2026; Received in revised form 29 May 2026; Accepted 16 June 2026
Available online 19 June 2026

anisotropy can be easily tailored upon several order of magnitude by simply changing the divalent cations, such as M = Zn(II), Ni(II), or Co(II) [5–7]. Moreover, the high crystal complementarity of spinel and wüstite phases when considering accurate chemical compositions results in high-quality epitaxial interfaces, which maximizes exchange coupling between hard and soft spins. Among a variety of core-shell nanoparticles combining spinel and wüstite phases as ferrimagnetic and anti ferromagnetic phases, which have been reported, one of the most investigated chemical structures are those made of CoO such as $Fe_{3-\delta}O_4$@CoO [8–11], CoO@Fe_3O_4 [12], CoO@$CoFe_2O_4$ [13,14]. CoO as wüstite fulfills the structural and magnetic prerequisites: its lattice parameter (a = 4.26 Å) [15] is almost exactly half of the spinel Fe_3O_4 (8.396 Å), giving a misfit below 2%, and its magnetocrystalline anisotropy constant ($K \approx 5 \times 10^6$ J m^{-3}) exceeds that of magnetite by two orders of magnitude. Seed-mediated growth yields coherently epitaxial Fe_3O_4@CoO nanoparticles in which the CoO shell pushes the median blocking temperature (T_B) up to the vicinity of the CoO Néel temperature (T_N = 293 K). Although this system contributed to prove the efficiency of exchange bias in core-shell nanoparticle, it remains limited by the order temperature of CoO which is below room temperature. Embedding Co/CoO clusters in a NiO matrix has already been shown to preserve the blocking of the ferromagnetic component far above the CoO T_N through AFM/AFM proximity effects, indicating that a NiO overlayer can supply a robust interfacial exchange field while simultaneously stabilising any residual CoO [16]. The proximity effect allows to trigger the magnetic order of CoO above its T_N (293 K) to that of NiO (525 K) [17], thus enabling exchange bias coupling at a soft-hard interface above the disordering temperature of the CoO AFM phase. Nevertheless, these effects seem to require large volumes of NiO, which is incompatible with the core-shell system at the nanoscale. An alternative strategy would be the formation of a NiO/CoO composite AFM shell, thus combining both high anisotropy of CoO and high ordering temperature of NiO [5].

Due to recent improvement of advanced techniques such as scanning transmission electron microscopy (STEM) combined with electron energy-loss spectroscopy (EELS) as well as X-ray absorption spectroscopy (XAS) and X-ray magnetic circular dichroism (XMCD), the spatial distribution of cations and their oxidation state can be precisely elucidated. Indeed, the structure of these nanoparticles is much more complex than the core-shell structure suggested by the size increase observed from TEM micrographs [18]. The high temperature (around 300 °C), which is mandatory to perform the thermal decomposition of metal complexes in order to grow metal oxides at the surface of pristine nanoparticles usually favors the interdiffusion of cations at the core-shell interface, leading to an intermediate layer with graded concentration from the interface [19–23]. Recently, we reported that the coexistence of an intermediate layer of $CoFe_2O_4$ and CoO shell behaves coherently as a single hybrid phase which combines high anisotropy of CoO and high magnetic order above room temperature of $CoFe_2O_4$ (Curie temperature T_C 570 K) [24]. Such proximity effects resulted in a blocked magnetic moment of $Fe_{3-d}O_4$@$CoFe_2O_4$/CoO@$Fe_{3-d}O_4$ nanoparticles well above room temperature without sacrificing the earth-abundant chemical composition and nanoparticle size below 20 nm.

In this context, we report on the synthesis of nanoparticles, which associate a Fe_3O_4 core at which surface the CoO shell is comforted by the formation of NiO. The synthesis pathway consists in a three-step seed-mediated synthesis. FeSt, CoSt and NiOct complexes were successively thermally decomposed in a high-boiling temperature solvent (310 °C) in order to incorporate Ni in the shell. A combination of high-resolution structural analysis including STEM-high-angle annular dark-field (HAADF) imaging, STEM-EELS and XAS-XMCD demonstrates the formation of a relatively complex chemical structure, which results from concomitant diffusion of cations at interfaces and partial solubilization-recrystallization mechanism. Magnetometry measurements showed that the distribution of Co and Ni in the structure of these nanoparticles significantly affect their magnetic properties.

2. Results and discussion

Nanoparticles were synthesized according to a three-step seed-mediated growth process which consists in the successive decomposition of metal precursors in presence of oleic acid in solution at high temperatures (Fig. 1). First of all, iron stearate (FeSt) was decomposed in dioctyl ether in order to synthesize iron oxide nanoparticles (Fe_3O_4). Second, cobalt stearate (CoSt) was decomposed in 1-octadecene in the presence of iron-oxide nanoparticles which were used as crystal seeds to form FeCo core-shell nanoparticles. Third, nickel octanoate (NiOct) was added to FeCo nanoparticles in order to be decomposed in octyl ether with an equimolar mixture of oleic acid and hexadecylamine to synthesize FeCoNi onion-type nanoparticles.

TEM micrographs (Fig. 2) show that nanoparticles display a shape being relatively close to a sphere for all steps of the synthesis process, from Fe_3O_4 to FeCo and FeCoNi nanoparticles. In contrast, the mean size of nanoparticles increases from 9.5 ± 1.1 nm for pristine Fe_3O_4 nanoparticles to 10.7 ± 1.2 nm for FeCo and 11.2 ± 1.3 nm for FeCoNi (Table 1). Although within the standart deviation this trend in size increase may agree with the growth of Co and Ni oxides, respectively. Energy-dispersive X-ray (EDX) spectrometry was also performed in order to get information on the relative atomic ratio of transition metals (Fe: Co: Ni) as depicted in Table 1. Obviously, the increase in size following the second synthesis step is clearly correlated with the presence of Co (36%) in FeCo. Although the Fe:Co ratio is preserved in FeCoNi, the amount of incorporated Ni is much lower (6%).

XRD patterns recorded for pristine Fe_3O_4, FeCo and FeCoNi nanoparticles show peaks that can be attributed to a spinel structure (Fig. 3a). Peaks become narrower after each successive thermal decomposition, attesting from the growth of crystal domains. Thanks to the Debye-Scherrer method, mean crystal sizes of 8.5, 9.3 and 9.8 nm were determined for Fe_3O_4, FeCo and FeCoNi, respectively, which agree with sizes measured from TEM and each nanoparticle as a single crystal. These values are slightly lower than values measured from TEM micrographs because latter consist in 2D projections of nanoparticles which usually leads to the overestimation of their size. The XRD pattern of FeCo shows an additional contribution around 36°, which corresponds to the presence of a wüstite structure. This contribution also exists in the pattern of FeCoNi although its intensity decreases with respect to that of FeCo. This behavior can be explained by the partial solubilization of CoO during the third thermal decomposition step, as previously reported [9,26]. As shown by EDX, the amount of NiO grown at the nanoparticle surface is not large enough to compensate for it. Cell parameters calculated for FeCo (8.399 ± 0.001 Å) and FeCoNi (8.414 ± 0.001 Å) are slightly larger than that of magnetite (8.396 Å, JCPDS card n° 19–062) in agreement with strains resulting from the slight difference between both cell parameters of CoO (4.263 Å) and NiO (4.178 Å) [26]. The cell parameter calculated for pristine iron oxide nanoparticles agrees with partial oxidation of Fe(II) at their surface as usually observed in the literature [27].

The chemical structure of nanoparticles was tentatively described through the vibration of the M-O bonds by performing FTIR measurements (Fig. 3b). A band centered to a frequency of 599 cm^{-1} was observed for FeCo which agree with M-O bonds in a spinel structure. This band is shifted to 591 cm^{-1} for FeCoNi which agree with some variation of the chemical composition. For pristine iron oxide nanoparticles, the observed broad band centered at 587 cm^{-1} agrees with partially oxidized magnetite ($Fe_{3-\delta}O_4$) [27]. The spectrum of FeCo shows an additional contribution at 725 cm^{-1} (indicated with a * in Fig. 3b), which is attributed to the stretching vibration mode of the Co—O bond in CoO [28]. The spectrum of FeCoNi also shows this band but with a lower intensity, which agrees with a lower amount of CoO although some NiO is formed as observed form the XRD pattern. These results confirm those obtained by XRD.

STEM-HAADF imaging was performed to obtain more precise information on morphology and crystal structure of the FeCo and FeCoNi

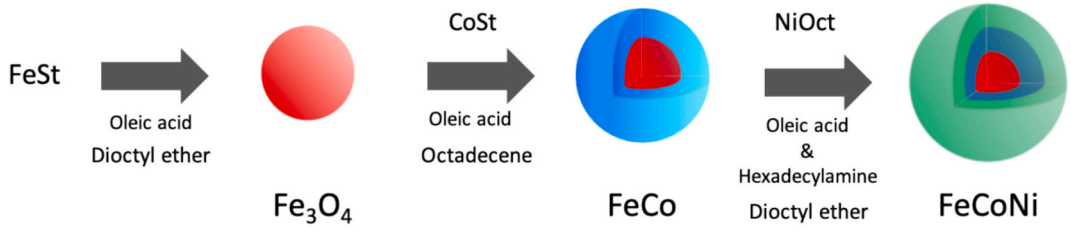

Fig. 1. Schematic illustration of the three-step synthesis pathway of FeCoNi nanoparticles.

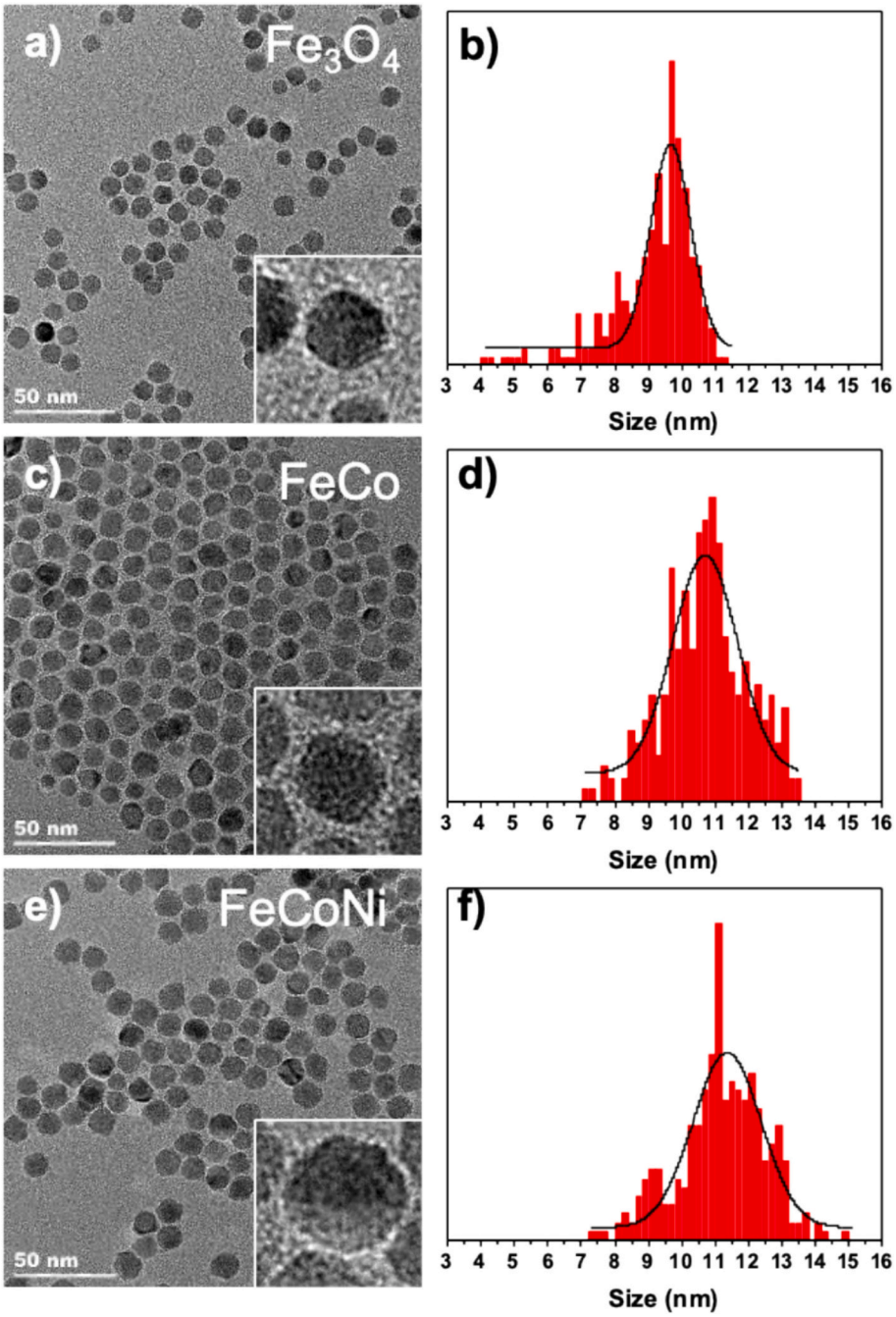

Fig. 2. TEM micrographs and corresponding size distributions of a,b) Fe_3O_4, c,d) FeCo and e,f) FeCoNi nanoparticles.

nanoparticles. Approximately half of the FeCo nanoparticles exhibit a round or slightly facetted shape (Fig. 4a). Nevertheless, the other half of nanoparticles display an irregular shape with some protrusion region (Fig. 4b), which can be attributed to some inhomogeneous growth of cobalt oxide. Both nanoparticles are designated as FeCo_r and FeCo_ir in the following. The surface of nanoparticles can be described as a

Table 1
Structural characteristics of nanoparticles.

		Fe_3O_4	FeCo	FeCoNi
TEM	**TEM size (nm)**	9.2 ± 1.2	10.7 ± 1.2	11.2 ± 1.3
	Relative size increase (nm)	_	+0.8	+0.3
XRD	**Crystal size (nm)**	8.5 ± 0.1	9.3 ± 0.1	9.8 ± 0.1
	Cell parameter (Å)	8.384 ± 0.001	8.399 ± 0.001	8.414 ± 0.001
TEM-EDX	**Fe: Co: Ni at. ratio (%)**	100: 0: 0	64: 36: 0	60: 34: 6

collection of facets corresponding to different crystallographic planes. Each *hkl* direction consists in different atom distributions and surface energy, the Co oxide may have grown selectively onto some facets. In both populations, continuous lattice fringes can be observed, in agreement with crystal structures. The fast Fourier transform (FFT) calculated for FeCo_r nanoparticles (inset in Fig. 4a) allows identifying the spinel structure in [110] orientation. The appearance of the FeCoNi nanoparticles is more homogeneous with a larger proportion of nanoparticles with homogeneous shape (Fig. 4c,d). FFT calculations show that the spinel structure is preserved (the inset in Fig. 4d corresponds to the [113] orientation). In addition, the protrusions of irregular nanoparticles seems to correspond to different lattice fringes although being less ordered which are expected to correspond to the wüstite structure as already reported [29]. Due to the small size of the protrusions in both samples and the similarity between the spinel and the wüstite structures, a clear identification of the crystal structure of this additional phase is hindered.

Spatially-resolved EELS spectrum-imaging was performed for those three types of nanoparticles in order to get a better insight on their chemical composition. Exemplary STEM-EELS data obtained from representative nanoparticles are shown in Fig. 5. For FeCo_r nanoparticles (Fig. 5a), the intensity distributions of oxygen, iron and cobalt clearly reveal the formation of a core-shell structure with an iron oxide core and a cobalt-iron oxide shell. The line profile across the nanoparticle reveals a clear increase in cobalt atomic concentration, which reaches up to more than 30 at.% at the very surface. Considering the chemical composition of the spinel ($CoFe_2O_4$, 14 Co at.%)) and the wüstite (CoO, 50 Co at.%) structure, we tentatively describe the core-shell structure as smooth transition from the Fe_3O_4 core to the CoO shell via $Co_xFe_{3-x}O_4$ composition. A shell thickness, corresponding to the Co graded composition, of 0.5 nm is observed.

In contrast, the data recorded for FeCo_ir nanoparticles (Fig. 5b) clearly shows an inhomogeneous Co distribution, which is preferentially located in two protrusion regions located at the surface of the iron oxide core. The Co content within this protrusion regions of about 0.5–2 nm reaches maximum values above 40 at. %, suggesting larger amount of CoO (in addition to $CoFe_2O_4$) than in FeCo_r nanoparticles. In addition to these protrusions, a very thin $Co_xFe_{3-x}O_4$ shell is still found at the very edge of the iron oxide core, suggesting that the core is fully covered with Co. STEM-EELS analysis of FeCoNi nanoparticles also correspond to two populations with different spatial distributions of cobalt (Fig. 5c). A comparison of the cobalt and nickel intensity maps clearly shows that Ni is preferentially located in protrusion regions with the highest Co content. This suggests that nickel oxide preferentially grows at the surface of CoO. Considering the low lattice mismatch beween CoO ($a = 4.263$ Å) and NiO ($a = 4.178$ Å) wüstite structures, most of Ni atoms may account from NiO. Nevertheless, Ni being spatially distributed on Co thin regions, a minor but non negligeable fraction may account to the spinel structure as $Ni_yCo_{1-y}Fe_2O_4$. Additionally, the population of FeCoNi nanoparticles with irregular shape is less pronounced compared to FeCo *nano*particles. It may be indicative of the spatial rearrangement of Co atoms upon the third thermal decomposition step as we already observed in similar systems [26]. The operating conditions favors the partial solubilization of CoO in Co monomers which certainly co crystallize with Ni monomers, resulting in the formation of Co Ni mixed ferrites at the surface of nanoparticles.

The chemical structure of these nanoparticles was investigated more locally by comparing EEL spectra from different regions of the spectrum images (Fig. 6). Sum spectra (Fig. 6a) reveal the presence of the ionization edges of the oxygen K (532 eV), the iron $L_{2,3}$ (710 eV), the cobalt $L_{2,3}$ (780 eV), and the nickel $L_{2,3}$ (855 eV) for FeCoNi. A detailed comparison of the energy-loss near-edge structure (ELNES) of the oxygen K edge for different regions of the nanoparticles is shown in Fig. 6b. The regions from which the spectra have been taken are marked by respectively colored frames in the dark-field images in Fig. 5. The spectrum recorded in the FeCo core is typical of magnetite (Fe_3O_4) with a sharp pre-peak followed by a valley and a broader maximum [30]. In contrast, the intensity of the pre-peak is relatively reduced in the spectra taken from the shells of the FeCo_r and FeCoNi nanoparticles, in agreement with a cobalt/nickel ferrite structure [31]. In the EEL spectrum taken from the cobalt-rich shell of the FeCo_ir nanoparticle, the significant reduction of the pre-peak intensity to a shoulder agrees with a different environment of oxygen atoms corresponding to CoO instead of cobalt ferrite [32,33]. This ELNES analysis is confirmed by the relative intensities of peaks recorded at iron and cobalt $L_{2,3}$ edges (Fig. 6c,d). The iron intensity is maximum for the core region, decreases for the FeCo_r shell and the FeCoNi shell and is minimum for the CoO -rich region in FeCo_ir (Fig. 6c). The cobalt content is maximum for the FeCo_ir shell

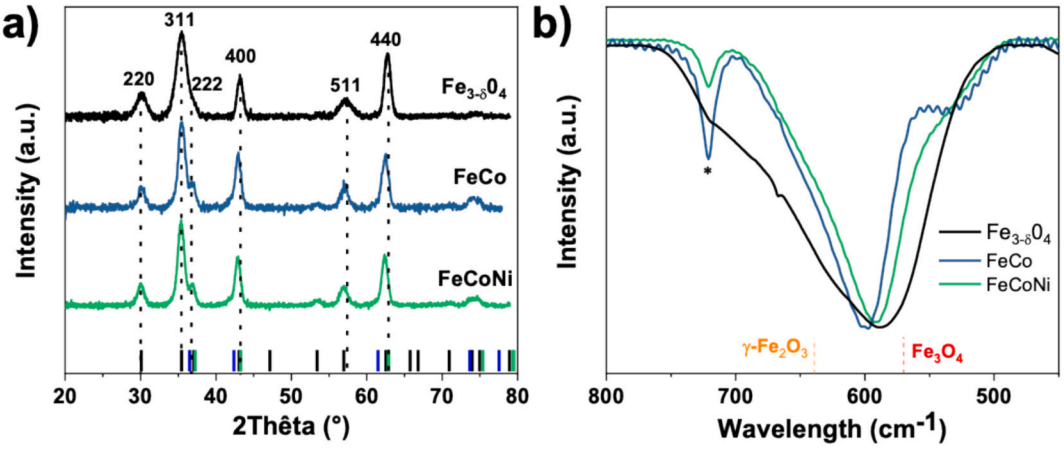

Fig. 3. a) XRD patterns of Fe_3O_4, FeCo and FeCoNi nanoparticles. Black, blue, and green bars correspond to Fe_3O_4 (JCPDS card n° 19–062), CoO (JCPDS card n° 70–2856), NiO (JCPDS card n° 47–1049) references. b) FTIR spectra of the low-wavelength region corresponding to M-O vibration modes. (For interpretation of the references to colour in this figure legend, the reader is referred to the web version of this article.)

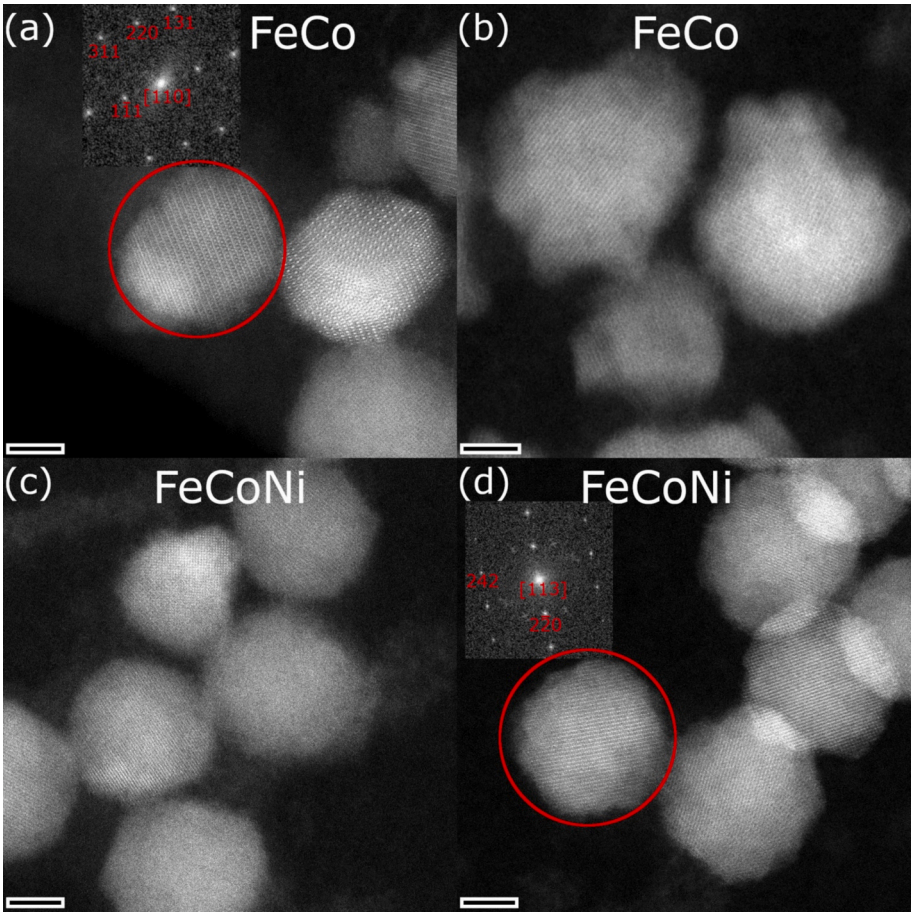

Fig. 4. STEM-HAADF images of (a,b) FeCo and (c,d) FeCoNi nanoparticles. FeCo nanoparticles with (a) a close-to sphere shape with continuous lattice fringes and (b) an irregular shape and regions with different lattice fringes within a single nanoparticle. FeCoNi nanoparticles appear with a slightly increased homogeneity but also exhibiting varying lattice-fringe contrast within single nanoparticles. Red circles in (a,d) indicate the image region from which the FFT has been calculated. Scale bars are (a,c,d) 4 nm and (b) 3nm and widths of FFT are 8.6 nm^{-1} in (b) and 14.3 nm^{-1} in (d). (For interpretation of the references to colour in this figure legend, the reader is referred to the web version of this article.)

and minimum for the FeCo core (Fig. 6d). The small amount of cobalt in the FeCo core is attributed to the thin shell present on top and bottom of the nanoparticle, which is seen in the spectrum that corresponds to a projection. The small amount of iron in the FeCo_ir shell could stem similarly from a small portion of core within the investigated region. In summary, EELS analysis suggests that the thin shell of the FeCo nanoparticles as well as the shell region of the FeCoNi nanoparticles correspond to a ferrite phase with varying amount of incorporated cobalt/nickel surrounding a magnetite iron oxide core. The thicker regions of the shell of the FeCo nanoparticles correspond well to a CoO phase.

In order to investigate in-depth the chemical structure of FeCo and FeCoNi, we performed XAS spectroscopy which is sensitive to the oxidation state of metals. XAS spectra recorded at the Fe $L_{2,3}$ edges are all typical of the iron oxide spinel structure (Fig. 7a) [25,34,35]. The I_1 and the I_2 peaks correspond to the contribution of Fe^{2+} in octahedral (O_h) sites and Fe^{3+} in (O_h) and (T_d) sites, respectively (Table 2). Hence, the I_1/I_2 ratio brings further information on the oxidation degree of magnetite ($I_1/I_2 = 0.71$) in maghemite ($I_1/I_2 = 0.35$) [36]. As expected, pristine iron oxide nanoparticles display an intermediate value (0.52), in agreement with the partial oxidation of Fe^{2+} at their surface. The formation of the CoO shell, results in the significant increase of the I_1/I_2 ratio (0.87) for FeCo, thus preventing further oxidation when exposed to air [37]. After the third synthesis step, the I_1/I_2 ratio decreases for FeCoNi which is rather unexpected since the formation of an extra shell should favor the stability of Fe^{2+}. Nevertheless, it can be attributed to the presence of Co(II) and Ni(II) in (O_h) sites of the spinel structure which reduce the Fe(II) /Fe(III) ratio. At the Co $L_{2,3}$ edges, the XAS spectrum depicts the presence of a significant fraction of CoO, according to the relative intensities of I_3 and I_4 peaks [37,38]. For FeCo and FeCoNi, $I_3/I_4 > 1$ which, according to the reference sample, agree with the presence of CoO. The decrease of this ratio from FeCo to FeCoNi attests from the reduction of the CoO fraction which benefits to cobalt ferrite (see below XMCD results). At the Ni $L_{2,3}$ edges, spectra of FeCoNi are typical of the Ni^{2+} in octahedral environment [39,40].

XMCD spectra was also performed to bring deeper insight on the oxidation state and site occupancy of cations (Fig. 7b,d,f). In contrast to XAS which probes all cations, XMCD only probes cations with uncompensated spins, i.e. which belong to the ferrimagnetic spinel structure, not the antiferromagnetic wüstite phase. At the Fe $L_{2,3}$ edges (Fig. 7b), typical signals of the spinel structure can be ascribed to Fe^{2+} and Fe^{3+} in O_h sites (S1 peak), Fe^{3+} in T_d site (S2 peak) and Fe^{3+} in (O_h) sites (S3 peak). Hence, the intensity S ratio (S1 + S2)/(S2 + S3) brings information on the chemical composition of the iron oxide phase (Table 2). It was calculated from ref [36] that a pure magnetite displays a value of 1.14 for this ratio while a pure maghemite displays a ratio of 0.69. Although similar values of the S ratio (0.83) were obtained for Fe_3O_4, FeCo and FeCoNi, it does correspond to different chemical structure. For pristine iron oxide nanoparticles, it corresponds to the partial oxidation of Fe^{2+} as observed from XAS. According to the reductive reaction medium, oxidized Fe cations at the surface of Fe_3O_4 nanoparticles should be reduced upon the second synthesis step. Obviously, a similar amount of Co(II) incorporate the spinel structure of FeCo nanoparticles which

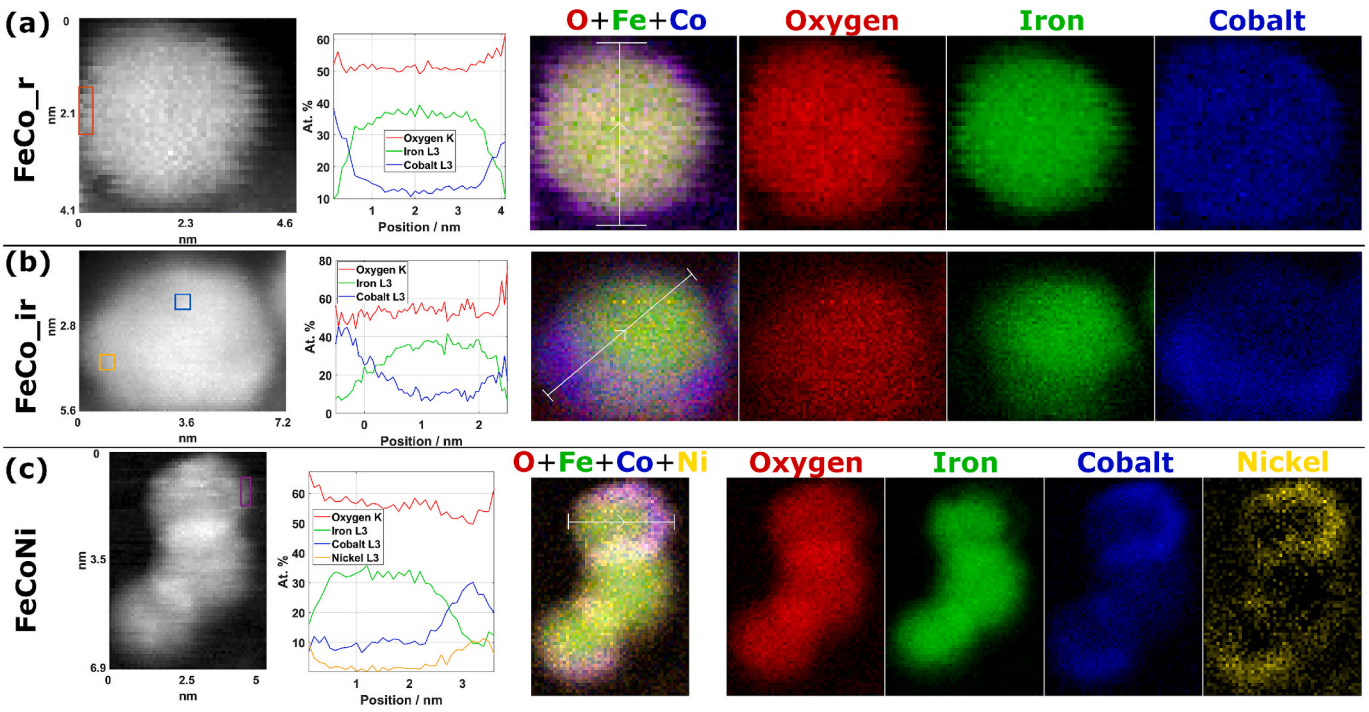

Fig. 5. Spatially resolved STEM-EELS analyses including dark-field images, concentration profiles and intensity maps of (a,b) a FeCo nanoparticle with (a) homogenous shape and (b) irregular shape and (c) FeCoNi nanoparticles. (a) FeCo_r nanoparticle which exhibits a homogeneous thin cobalt shell with the cobalt content at the very surface reaching 30 at.%. (b) FeCo_ir nanoparticle which shows an inhomogeneous Co distribution in two regions with increased cobalt content of up to 40 at.%. (c) The analysis of the FeCoNi nanoparticles shows that the nickel and cobalt contents have a positive correlation, indicating that the Ni oxide grew preferentially at the surface of the cobalt-rich regions. The colored frames shown in the DF images indicate the regions from which EEL spectra (Fig. 6) have been extracted.

result in the formation of cobalt ferrite at the Fe_3O_4/CoO interface [37]. For FeCoNi, the unchanged value of the S ratio agree with the similar occupation of O_h sites by Co^{2+} or Ni^{2+} to that of Fe^{2+}. Upon each synthesis step, the nanoparticle structure undergoes significant rearrangement. From XAS spectra, the surprising decrease of the I1/I2 ratio from FeCo to FeCoNi results from the partial incorporation of Co(II) in the spinel structure, thus contributing to decrease the Fe(II)/Fe(III) ratio. The incorporation of Ni(II) in the spinel phase also contributes to this result.

At the Co and Ni $L_{2,3}$ edges (Fig. 7d,f), negative peaks were observed, in agreement with the occupancy of O_h sites by Co^{2+} [41] and Ni^{2+} [39,40] in the spinel structure. Considering the XAS threshold, the fraction of uncompensated spins of Co^{2+} increases from 22% in FeCo to 43% in FeCoNi (Table 2). The fraction of Ni^{2+} uncompensated spins is significant in FeCoNi (22%), in agreement with its incorporation to a spinel structure through partial solubilization-recrystallization mechanism. It is worth noting that, as shown by the CoO reference sample (Fig. 7d), a substantial fraction of Co and Ni uncompensated spin may account from the surface because of symmetry break [37]. Nevertheless, the majority of Co^{2+} (57%) and Ni^{2+} (78%) are still part of the wüstite phase (Table 2).

During each synthesis step the high temperature (about 300 °C) favors the rearrangement of cation through diffusion at the core-shell interface [37,42] or surface rearrangement through partial solubilization-recrystallization [9,26]. In the case of FeCo, it favors the formation of cobalt ferrite while CoO decreases as observed from XRD patterns and FTIR spectra. The respective amounts of each phase were quantified by comparing the intensity at the energy threshold at the Co $L_{2,3}$ edge in XAS and XMCD spectra. The S ratio also indirectly brings some information since it remains constant to that of pristine iron oxide nanoparticles. According to the reductive reaction medium, partially oxidized Fe cation at the surface of nanoparticles should be reduced. Therefore, a similar amount of Co(II) incorporate the spinel structure and result in the formation of cobalt ferrite at the Fe_3O_4/CoO interface [37].

Upon the third thermal decomposition step, this phenomenon certainly continue while Ni monomers also participate. Although most of them form NiO (or $Co_{0.5}Ni_{0.5}O$ through partial solubilization-recrystallization process) at the surface of CoO rich region of FeCo, a minor contribution is also incorporated in the spinel structure as $Ni_yCo_{1-y}Fe_2O_4$ as shown by the XMCD peak recorded at the Ni $L_{2,3}$ edge. According to the S ratio and the Fe $L_{2,3}$ edge XCMD spectrum, the incorporated amount compensates the reduced Fe(III).

Element specific XMCD M(H) curves were recorded in order to get information on the magnetic structure of these nanoparticles, more precisely the exchange coupling between cations occupying the O_h sites of the spinel structure. Curves recorded at 4.2 K for FeCo and FeCoNi nanoparticles at the Fe S3, Co S4, Ni S5 edges all showed hysteresis (Fig. 8a). Coercive fields calculated for FeCo nanoparticles at the Fe S3 and Co S4 edges (8.6 and 6.6 kOe, respectively) correspond the relatively strong exchange coupling between uncompensated spins of Fe^{3+} and Co^{2+} occupying (O_h) sites of a spinel structure. M(H) curves recorded for FeCoNi also show hysteresis loops at the Fe S3 and Co S4 edges (Fig. 8b). H_C values corresponding to Fe S3 and Co S4 edges of FeCoNi nanoparticles higher (9.5 and 9.0 kOe, respectively) which agree with stronger exchange coupling, probably because there is a larger amount of Co^{2+} in the spinel structure. At the NiS5 edge, the value of H_C (7.6 kOe) also agree with exchange coupling between Ni, Co and Fe atoms and reflects the moderate amount of Ni^{2+} in the spinel structure.

The different values of H_C for different elements of the same nanoparticles can be explained by different populations of cations with uncompensated spins. First, some uncompensated spins of Fe^{3+} belong to the Fe_3O_4 core. Because they are pined with other Fe^{3+} exchange coupling is stronger. Second, some Co and Ni uncompensated spins are localized at the surface of nanoparticles, whether in spinel or wüstite structure. Because of the break of symmetry at the nanoparticle surface

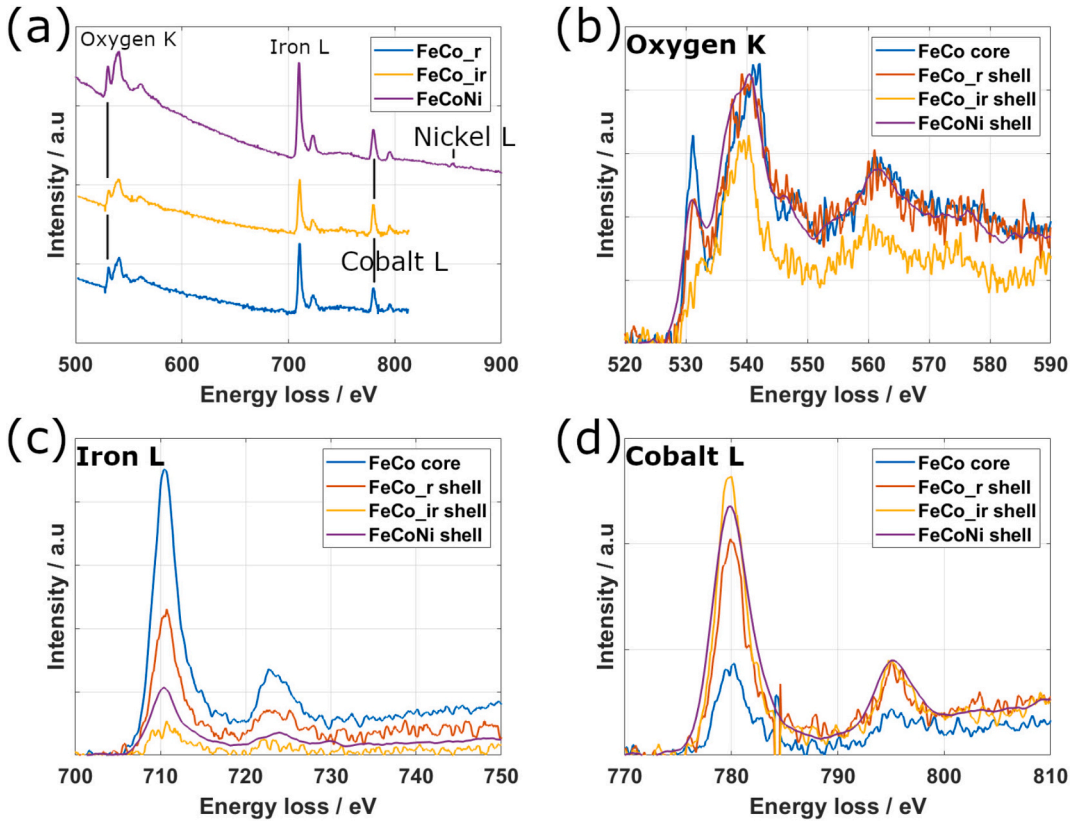

Fig. 6. EEL spectra taken from the STEM-EELS analyses shown in Fig. 5. (a) Comparison of the sum spectra of the three spectrum images shown in Fig. 5 revealing the oxygen *K*, iron $L_{2,3}$, cobalt $L_{2,3}$ edges and in the case of the FeCoNi nanoparticle also the nickel $L_{2,3}$ edge. (b-d) Comparison of the (b) oxygen *K*, (c) iron $L_{2,3}$ and (d) cobalt $L_{2,3}$ edges spectra taken from different regions of the nanoparticles: core (blue lines) and shell (red) regions of the *FeCo_r* nanoparticle, protrusion regions of the *FeCo_ir* nanoparticle (yellow) and shell region of the *FeCoNi* nanoparticle (purple). The spectra of the FeCo nanoparticles are shown as is, the FeCoNi spectra, taken with a different beam current, have been normalized with respect to the O K edge. (For interpretation of the references to colour in this figure legend, the reader is referred to the web version of this article.)

which induced surface spin glass, they remain unpinned and do not contribute to exchange coupling [43]. In addition, the values of the magnetic moments show that the amount of uncompensated spin of Fe and Co are similar whereas it is half for Ni in agreement with the lower fraction of Ni in the spinel structure.

Magnetic properties of FeCo and FeCoNi nanoparticles were investigated by SQUID magnetometry and compared to those of pristine iron oxide nanoparticles (Table 3). Temperature dependent magnetization curves (M(T)) recorded after cooling down under zero field (ZFC) show a maximum, usually ascribed to the blocking temperature (T_{MAX}) were the magnetic anisotropy energy (KV, where K is the magnetic anisotropy constant and V is the volume of nanoparticles) of the system equals the thermal energy ($25k_BT$, where k is the Boltzmann constant and T is the temperature) (Fig. 9a). Above T_{MAX}, the magnetic moment oscillates along the magnetization axis, e.g. the superparamagnetic behavior. Considering that such magnetic transition is dependent on the size and shape distributions, the blocking temperature can be described more accurately by considering a distribution of temperature such as: [44]

$$f(T_B) = d(M_{ZFC} - M_{FC})/dT$$

As the samples being measured in the powder state, strong dipolar interactions increase T_{MAX} [45,46]. Nevertheless, nanoparticles remain covered by surfactant, avoiding direct contact between them. The nanoparticles volume and magnetic moment being of the same order of magnitude, we considered that dipolar interactions are relatively similar in all samples. T_B calculated for FeCo (252 K) and FeCoNi (259 K) are much higher than that of pristine iron nanoparticles (65 K), which agree with significant increase of magnetic anisotropy energy (Fig. 9b). M(T) curves recorded after cooling down under a magnetic field of 75 Oe, agree with such transition from blocked magnetic moments to superparamagnetic behavior around T_B since the net magnetization starts to softly decrease far before T_{MAX} and become more intense when getting closer to it.

Magnetization curves recorded at 300 K against an applied magnetic field showed perfect overlapping of each branch, thus confirming the superparamagnetic behavior for all three samples (Fig. 10a). In contrast, zero field cooled (ZFC) M(H) curves recorded at 5 K clearly show hysteresis which agree with blocked magnetic domains (Fig. 10b). While the coercive field (H_C) of pristine iron oxide nanoparticles is low (441 Oe), FeCo with a spinel@wüstite structure leads to a significant increase up to 20.5 kOe which belong to the highest values measured for this class of nanoparticles [8,22] [47]. Exchange bias coupling is favored between the spinel core and the CoO shell grown at their surface as observed on EELS images. Moreover, smooth curves attest from the coherent rotation of fully coupled spins through exchange interactions at the interface of the soft core and the hard shell upon magnetic reversal. A lower values of 18 kOe was calculated for FeCoNi because of the lower fraction of CoO as mentioned above. In addition, NiO having lower magnetic anisotropy results in less efficient exchange coupling.

These results were confirmed by field cooled (FC) M(H) curves recorded at 10 K after cooling down under a magnetic field (7 T) (Fig. 10c). H_C values of both FeCo and FeCoNi are higher than those of the ZFC M(H) curves due to the exchange coupling with pinned uncompensated high-anisotropy spins at the soft–hard interfaces. The increase is higher for FeCo than FeCoNi because of the larger fraction of uncompensated spins of CoO [24,48]. The horizontal shift of the hysteresis loop down to negative magnetic fields is ascribed to the pinning of soft Fe_3O_4 spins by the uncompensated spins of the CoO phase, which

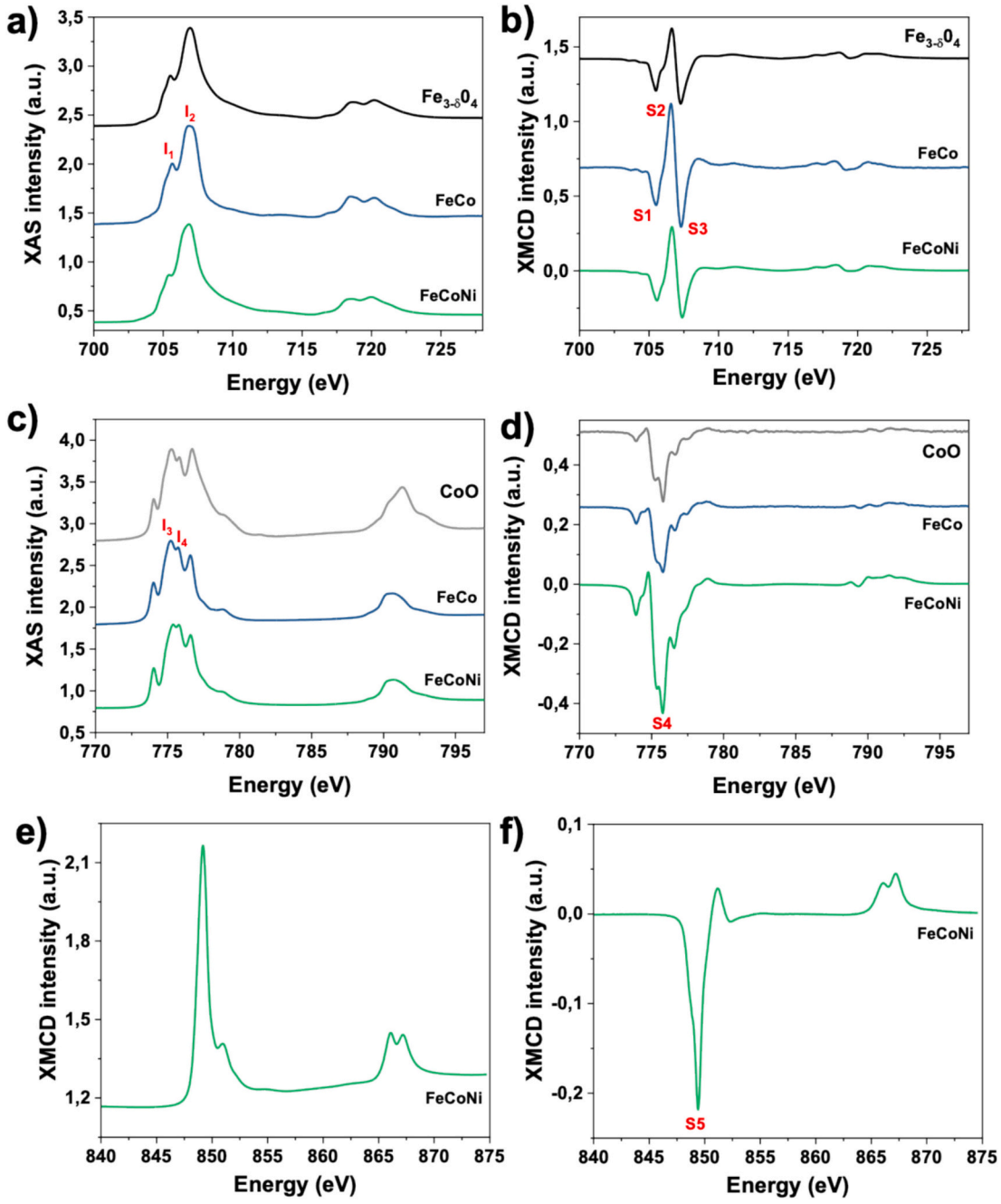

Fig. 7. a,c,e) Isotropic XAS and b,d,f) XMCD spectra recorded at the Fe $L_{2,3}$ edges for $Fe_{3-\delta}O_4$, FeCo and FeCoNi nanoparticles. a, b) Fe $L_{2,3}$ edges, c,d) Co $L_{2,3}$ edges and e,f) Ni $L_{2,3}$ edges. All XAS and XMCD were normalized by the jump of edge of isotropic XAS.

Table 2
XAS and XMCD structural characteristics of samples.

Sample	Size (nm)	I_1/I_2	(S1 + S2)/(S2 + S3)	I_3/I_4	S4 (%)	S5 (%)
Fe_3O_4	10.1	0.56	0.83	–	–	–
FeCo	10.7	0.87	0.82	1.11	22	–
FeCoNi	11.2	0.63	0.82	1.01	43	22
Magnetite [25]	–	0.71	1.14		–	–
Maghemite [25]	–	0.35	0.69		–	–

aligned with the magnetic field upon cooling down, establishing a unidirectional anisotropy. The associated exchange field (H_E) is pretty huge (2.1 kOe) for FeCo consistently with strong exchange bias coupling which involved the high fraction of uncompensated spins of CoO. Nevertheless, H_E decreases to 1.6 kOe for FeCoNi as a result of the partial conversion of CoO to $CoFe_2O_4$ which lacks such pinned uncompensated spins. Probably the intermixing of Ni^{2+} with CoO contributes to the lower H_E since it results in lower magnetic anisotropy. The hysteresis cycle of FeCo is also vertically shifted as usually observed for exchange coupled nanoparticles were a significant fraction of Co spins remains uncompensated [49]. Due to the lower content of CoO in FeCoNi, the vertical shift is less significant. Moreover, the non-saturation of M(H) curves at 7 T attests from the significant increase of effective magnetic anisotropy which results from the exchange coupling between the soft core and the hard shell.

Considering the rather limited volume increase between Fe_3O_4 and FeCo nanoparticles, such a huge increase of T_B is ascribed to exchange

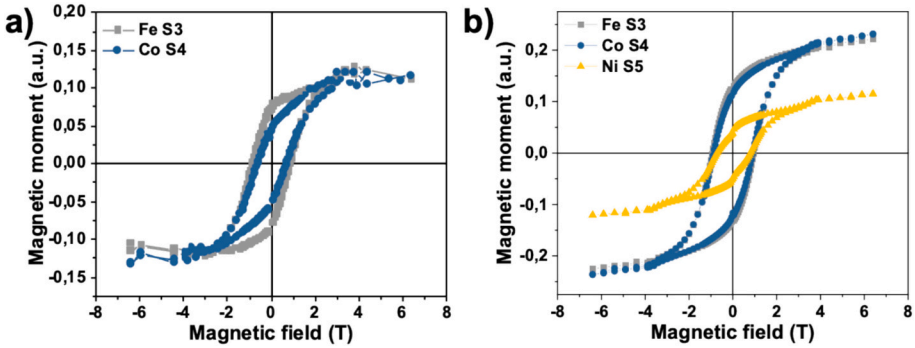

Fig. 8. Element specific XMCD M(H) curves recorded at 4 K at Fe S3, Co S4 and Ni S5 edges for a) FeCo and FeCoNi nanoparticles.

Table 3
Magnetic characteristics of $Fe_{3-\delta}O_4$, FeCo and FeCoNi nanoparticles.

	Fe_3O_4	FeCo	FeCoNi
TEM size (nm)	9.2 ± 1.2	10.7 ± 1.2	11.2 ± 1.3
Size variation (nm)	_	0.8	0.3
Shell volume (nm^3)	_	234	94
H_C 5 K FC (kOe)	0.44	22.6	18.9
H_E 5 K FC (kOe)	0.14	2.1	1.6
T_{max} FC-ZFC (K)	121	294	294
T_B d(MZFC-MFC)/dT (K)	65	252	259
K_{eff} (10^5 J/m^3)	1.0	1.4	1.2

bias coupling at the interface between the soft Fe_3O_4 phase ($K_{Fe3O4} = 4.6.10^4$ J.m^{-3}) [50] and both hard CoO ($K_{CoO} = 7.10^6$ J.m^{-3}) [51] and ($CoFe_2O_4$ $K_{CoFe2O4} = 3.10^5$ J.m^{-3}) [52] phases. The pinning of soft by the hardest spins at the core-shell interface results in an extra anisotropy energy. As we already observed in similar nanoparticles, T_{MAX} corresponds to the Néel temperature ($T_N = 290$ K) of CoO above which the AFM order does not exist, e.g. the effective pinning of soft spins of the core. Moreover, the increase of magnetization from 100 K to the onset of the ZFC peak suggests that the AFM order is lost in the thinnest area of CoO due to size effect [53]. It is confirmed by a contribution of T_B centered to 120 K (Fig. 9b). This behavior is not observed for the FeCoNi nanoparticles, in agreement with the conversion of the thinnest CoO areas by partial solubilization-recrystallization process. After the third synthesis step, the increase of T_B for FeCoNi is very limited. It can be explained by the very limited amount of Ni with respect to that of Co as shown by EDX and EELS leading to very thin layers of NiO and $NiFe_2O_4$ with low magnetic anisotropy ($K_{NiO} = 8.10^3$ J/m^3) [54] and $K_{NiFe2O4} = -6.7.10^3$ J.m^{-3}) which suggest that they do not contribute to the increase of T_B.

As shown by element specific XMCD curves, the fraction of Co uncompensated spins increases according to the conversion of CoO in $CoFe_2O_4$ driven by rearrangement processes. It is worth noting that, although the significant reduction of the CoO phase from 78% to 57% as revealed by XMCD, it does not affect the magnetic anisotropy energy of the nanoparticles. It seems that although the $CoFe_2O_4$ hard phase which

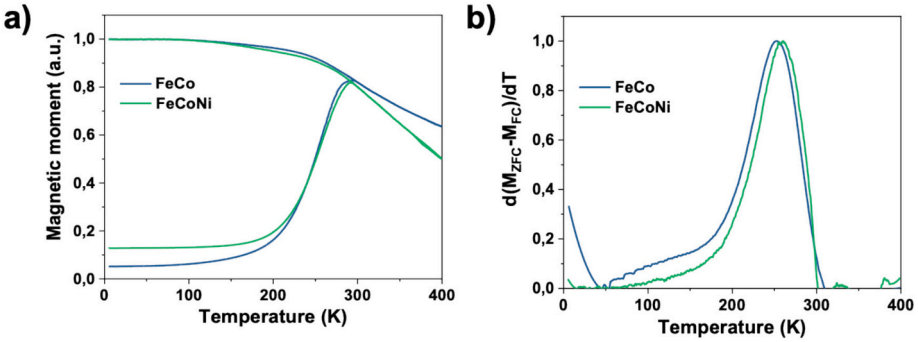

Fig. 9. a) Temperature dependent magnetization curves recorded for FeCo and FeCoNi nanoparticles and b) the corresponding distribution of T_B.

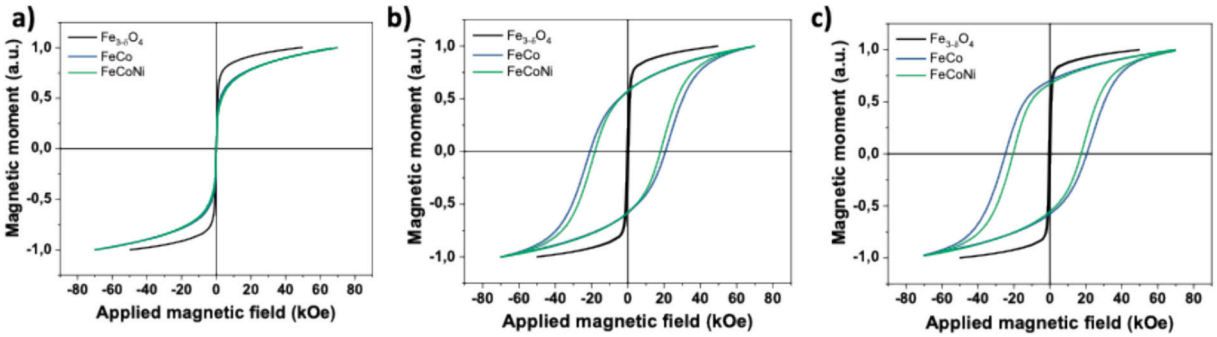

Fig. 10. Magnetization curves recorded against an applied magnetic field for $Fe_{3-\delta}O_4$, FeCo and FeCoNi nanoparticles a) at 300 K, b) at 5 K after zero field cooling and c) at 5 K after field cooling at 7 T.

results from the conversion of CoO has a lower magnetic anisotropy, it is sufficient to compensate the loss of exchange bias coupling by dual exchange coupling [26]. Indeed the formation of $CoFe_2O_4$ favors higher spin orbit coupling of Fe and Co which contributes to the magnetic anisotropy [22]. Recently, we reported on the proximity effect between both CoO and $CoFe_2O_4$ which resulted in the significant enhancement of T_B above room temperature [24]. Both phases behave coherently as an hybrid phase which combines both high anisotropy and ordering temperature. However, the conversion of CoO in $CoFe_2O_4$ is not sufficient to allow and effective interface which induces proximity effect between both phases. [24] In contrast, a significant fraction of Ni compensated spins remains probably at the NiO surface. Although the Néel temperature is much higher than that of CoO, its relatively low amount has no significant influence on magnetic anisotropy of FeCoNi nanoparticles. Indeed the incorporation of Ni in the shell structure probably led to intermixed phases such as $Ni_xCo_{1-x}O$ as suggested by STEM-HAADF micrographs and EELS mapping which may hamper the proximity effect due to inefficient contribution of its Néel temperature.

3. Conclusion

We have reported on the synthesis of core-shell nanoparticles by performing a three-step synthesis process. As we reported earlier, the synthesis of core-shell nanoparticles through successive thermal decompositions of metal complexes is a very complex mechanism [24,26]. First of all, Co diffuses homogeneously at the surface of the Fe_3O_4 nanoparticles in order to result in a spinel structure with graded Co concentration from the surface. Although Fe_3O_4 nanoparticles may be considered as spheres, their surface consists in a collection of facets with specific *hkl* reflections and surface energy. Therefore, it favors the inhomogeneous growth of a metal oxide wüstitewü shell at their surface, resulting in irregular shape. As shown by STEM and EELS, the structure of nanoparticles can be described as a Fe_3O_4 core which belongs to the spinel phase with an inhomogeneous shell which consists in protrusions correlated to a wüstite CoO phase. Secondly, the shell formation happens at a high temperature (about 300 °C) and thus favors complex mechanisms during the synthesis such as diffusion of cations at the interface of both Fe_3O_4 and CoO phase leading to the formation of an intermediate cobalt ferrite phase. It can also be ascribed to the partial solubilization of the Fe_3O_4 core followed by the co-crystallization of released Fe monomers with added Co monomers. Once all Fe monomers were consumed, CoO formation takes place on specific facets of the nanoparticles. Therefore, uncovered areas consist in a relatively thin Co-dopped ferrite surface as shown by STEM-HAADF imaging and EELS mapping. Thirdly, surface rearrangement was clearly observed after the third synthesis step which led to nanoparticles with less irregular shapes. XRD and FTIR revealed that the contribution of the wüstite phase decreased and is concomitant to the expansion of the cobalt/nickel ferrite phase. The experimental conditions favor the partial solubilization of CoO which crystallizes in spinel phase as shown by EELS spectra of the oxygen K edge and XCMD of Fe and Co edges. Nevertheless, this mechanism also involves the reaction of Ni monomers which results from the thermal decomposition. Although the amount of Ni is less than that of Co, NiO forms preferentially at the surface of Co rich region thanks to high crystal complementarity between both wüstite phases (CoO and NiO) as shown by EELS spectrum imaging and XMCD. Therefore, we may expect some diffusion at the interface leading to $Ni_xCo_{1-x}O$ intermediate phase. XMCD also revealed that Ni is also part of the spinel structure, leading to an intermediate $Ni_yCo_{1-y}Fe_2O_4$ phase. Therefore, the chemical structure of FeCo and FeCoNi nanoparticles can be described as a Fe_3O_4 spinel core surounded with varying amount of incorporated cobalt/ nickel and a discontinuous $Ni_xCo_{1-x}O$ wüstite shell, both with intermixed graded chemical compositions.

The coexistence of both spinel and wüstite phases results in a hybrid phase, whose chemical composition controls the magnetic efficiency of the associated proximity effect. In contrast to our previous study [24], the volume ratio between $CoFe_2O_4$ and CoO ratio is not high enough to allow the proximity effect which results in the shift of T_B beyond room temperature. The formation of cobalt ferrite only compensates the loss of magnetic anisotropy energy resulting from the reduction of the CoO volume. In our previous work [24], the conversion of CoO in $CoFe_2O_4$ was driven by the amount of the FeSt complex used for the third thermal decomposition. Fe monomers resulting from the decomposition of FeSt seem to favor the conversion of CoO upon partial solubilization at its surface, thus increasing the $Co_xFe_{3-x}O_4$/CoO interface, which enhances the proximity effect of the hybrid phase. In this study, it seems that the use of NiOct complex instead of FeSt is not appropriate to drive the formation of such a hybrid phase because of the resulting $Ni_yCo_{1-y}FeO_4$ phase having a lower magnetic anisotropy.

Consequently, Fe_3O_4@$Ni_yCo_{1-y}Fe_2O_4$/$Ni_xCo_{1-x}O$ nanoparticles which include a hybrid phase, which favors proximity effects represent an attractive approach in the quest for rare-earth-free nanomagnets with finely tunable anisotropy and thermal stability. Their design leverages structurally compatible, earth-abundant components to overcome intrinsic temperature limitations, opening pathways to scalable and sustainable magnetic nanomaterials for advanced functional applications.

CRediT authorship contribution statement

Kevin Sartori: Writing – original draft, Methodology, Investigation, Formal analysis, Data curation. **Fadi Choueikani:** Writing – review & editing, Supervision, Resources, Investigation, Funding acquisition, Formal analysis, Data curation. **Simon Hettler:** Writing – review & editing, Resources, Formal analysis, Data curation. **Raul Arenal:** Writing – review & editing, Resources, Formal analysis, Data curation. **Benoit P. Pichon:** Writing – review & editing, Writing – original draft, Validation, Supervision, Resources, Project administration, Methodology, Investigation, Funding acquisition, Formal analysis, Conceptualization.

Declaration of competing interest

The authors declare that they have no known competing financial interests or personal relationships that could have appeared to influence the work reported in this paper.

Acknowledgment

K.S. was supported by a PhD grant from the French Agence Nationale de la Recherche (ANR) under the reference ANR-11-LABX-0058-NIE within the Investissement d'Avenir program ANR-10-IDEX-0002-02 and SOLEIL synchrotron / Laboratoire Léon Brillouin fellowship. The authors are grateful to SOLEIL synchrotron light source for providing the access to DEIMOS beamline and to DIAMOND synchrotron light source for providing access to BLADE beamline. R.A. and S.H. acknowledge funding from the Spanish MICIU (PID2023-151080NB-I00/AEI/10.13039/501100011033) and CEX2023-001286-S MICIU/AEI /10.13039/501100011033) as well from the Gobierno de Aragón (DGA) under project E13-23R. STEM imaging and spectroscopic (EELS) studies have been conducted in the Laboratorio de Microscopias Avanzadas (LMA) at Universidad de Zaragoza.

Appendix A. Supplementary data

Supplementary data to this article can be found online at https://doi.org/10.1016/j.jmmm.2026.174343.

Data availability

Data will be made available on request.

References

[1] O. Gutfleisch, M.A. Willard, E. Brück, C.H. Chen, S.G. Sankar, J.P. Liu, Adv. Mater. 23 (2011) 821–842.
[2] Magnetic Relaxation in Fine-Particle Systems, Dormann, Advances in Chemical Physics, Wiley Online Library, 1997. https://onlinelibrary-wiley-com.scd-rproxy.u-strasbg.fr/doi/10.1002/9780470141571.ch4 (accessed June 25, 2025).
[3] S. Bedanta, W. Kleemann, J. Phys. D. Appl. Phys. 42 (2008) 013001.
[4] A. López-Ortega, M. Estrader, G. Salazar-Alvarez, A.G. Roca, J. Nogués, Phys. Rep. 553 (2015) 1–32.
[5] A. Mandziak, G.D. Soria, J.E. Prieto, P. Prieto, C. Granados-Miralles, A. Quesada, M. Foerster, L. Aballe, J. de la Figuera, Sci. Rep. 9 (2019) 13584.
[6] E. Fantechi, G. Campo, D. Carta, A. Corrias, C. de Julián Fernández, D. Gatteschi, C. Innocenti, F. Pineider, F. Rugi, C. Sangregorio, J. Phys. Chem. C 116 (2012) 8261–8270.
[7] V. Mameli, A. Musinu, A. Ardu, G. Ennas, D. Peddis, D. Niznansky, C. Sangregorio, C. Innocenti, N.T.K. Thanh, C. Cannas, Nanoscale 8 (2016) 10124–10137.
[8] X. Liu, B.P. Pichon, C. Ulhaq, C. Lefèvre, J.-M. Grenèche, D. Bégin, S. Bégin-Colin, Chem. Mater. 27 (2015) 4073–4081.
[9] T. Gaudisson, R. Sayed-Hassan, N. Yaacoub, G. Franceschin, S. Nowak, J.-M. Grenèche, N. Menguy, Ph. Sainctavit, S. Ammar, CrystEngComm 18 (2016) 3799–3807.
[10] G. Franceschin, T. Gaudisson, N. Menguy, B.C. Dodrill, N. Yaacoub, J.-M. Grenèche, R. Valenzuela, S. Ammar, Part. Part. Syst. Charact. 35 (2018) 1800104.
[11] I. Panagiotopoulos, G. Basina, V. Alexandrakis, E. Devlin, G. Hadjipanayis, L. Colak, D. Niarchos, V. Tzitzios, J. Phys. Chem. C 113 (2009) 14609.
[12] A. López-Ortega, B. Muzzi, C. de Julián Fernández, C. Sangregorio, ACS Appl. Nano Mater. 7 (2024) 27489–27497.
[13] G.C. Lavorato, D. Peddis, E. Lima, H.E. Troiani, E. Agostinelli, D. Fiorani, R. D. Zysler, E.L. Winkler, J. Phys. Chem. C 119 (2015) 15755–15762.
[14] G.C. Lavorato, E.L. Jr, D. Tobia, D. Fiorani, H.E. Troiani, R.D. Zysler, E.L. Winkler, Nanotechnology 25 (2014) 355704.
[15] W.L. Roth, Phys. Rev. 110 (1958) 1333–1341.
[16] J.A. De Toro, D.P. Marques, P. Muñiz, V. Skumryev, J. Sort, D. Givord, J. Nogués, Phys. Rev. Lett. 115 (2015) 057201.
[17] H. Bilz, W. Kress, Phonon Dispersion Relations in Insulators, Springer, Berlin, Heidelberg, 1979, pp. 49–57.
[18] K. Sartori, A. Musat, F. Choueikani, J.-M. Grenèche, S. Hettler, P. Bencok, S. Begin-Colin, P. Steadman, R. Arenal, B.P. Pichon, ACS Appl. Mater. Interfaces 13 (2021) 16784–16800.
[19] A. Juhin, A. López-Ortega, M. Sikora, C. Carvallo, M. Estrader, S. Estradé, F. Peiró, M. Dolors Baró, P. Sainctavit, P. Glatzel, J. Nogués, Nanoscale 6 (2014) 11911–11920.
[20] S. Lentijo-Mozo, D. Deiana, E. Sogne, A. Casu, A. Falqui, Chem. Mater. 30 (2018) 8099–8112.
[21] A. Uheida, G. Salazar-Alvarez, E. Björkman, Z. Yu, M. Muhammed, J. Colloid Interface Sci. 298 (2006) 501–507.
[22] E. Skoropata, R.D. Desautels, C.-C. Chi, H. Ouyang, J.W. Freeland, J. van Lierop, Phys. Rev. B 89 (2014) 024410.
[23] E. Tronc, J.-P. Jolivet, J. Lefebvre, R. Massart, J. Chem. Soc. Faraday Trans. 1 Phys. Chem. Condens. Phases 80 (1984) 2619.
[24] K. Sartori, R. Lopez-Martin, F. Choueikani, A. Gloter, J.-M. Grenèche, S. Begin-Colin, D. Taverna, J.A.D. Toro, B.P. Pichon, Nanoscale Adv. 6 (2024) 2903–2918.
[25] S. Brice-Profeta, M.-A. Arrio, E. Tronc, N. Menguy, I. Letard, C. Cartier dit Moulin, M. Noguès, C. Chanéac, J.-P. Jolivet, Ph. Sainctavit, J. Magn. Magn. Mater. 288 (2005) 354–365.
[26] K. Sartori, D. Ihiawakrim, C. Lefèvre, S. Reguer, C. Mocuta, S. Bégin-Colin, F. Choueikani, B.P. Pichon, Mater. Adv. 3 (2022) 8716–8728.
[27] W. Baaziz, B.P. Pichon, S. Fleutot, Y. Liu, C. Lefevre, J.-M. Greneche, M. Toumi, T. Mhiri, S. Begin-Colin, J. Phys. Chem. C 118 (2014) 3795–3810.
[28] C.-W. Tang, C.-B. Wang, S.-H. Chien, Thermochim. Acta 473 (2008) 68–73.
[29] I. Makarchuk, B. Rotonnelli, L. Royer, S. Hettler, J.-J. Gallet, F. Bournel, J. Guehl, A. Brige, A. Zitolo, G. Kéranguéven, A. Bonnefont, R. Arenal, E. Savinova, T. Asset, B.P. Pichon, Chem. Mater. 37 (2025) 833–844.
[30] A. Gloter, M. Zbinden, F. Guyot, F. Gaill, C. Colliex, Earth Planet. Sci. Lett. 222 (2004) 947–957.
[31] S. Hettler and R. Arenal, Micron, 2025, 196–197, 103858.
[32] D. Barreca, A. Gasparotto, O.I. Lebedev, C. Maccato, A. Pozza, E. Tondello, S. Turner, G.V. Tendeloo, CrystEngComm 12 (2010) 2185–2197.
[33] Z.-W. Gao, T. Ma, X.-M. Chen, H. Liu, L. Cui, S.-Z. Qiao, J. Yang, X.-W. Du, Small 14 (2018) 1800195.
[34] X. Zhu, S.S. Kalirai, A.P. Hitchcock, D.A. Bazylinski, J. Electron Spectrosc. Relat. Phenom. 199 (2015) 19–26.
[35] T.E. Torres, A.G. Roca, M.P. Morales, A. Ibarra, C. Marquina, M.R. Ibarra, G. F. Goya, J. Phys. Conf. Ser. 200 (2010) 072101.
[36] E. Pellegrin, et al., Phys. Status Solidi 215 (1999) 797.
[37] K. Sartori, G. Cotin, C. Bouillet, V. Halte, S. Begin-Colin, F. Choueikani, B. P. Pichon, Nanoscale 11 (2019) 12946–12958.
[38] S.Y. Istomin, O.A. Tyablikov, S.M. Kazakov, E.V. Antipov, A.I. Kurbakov, A. A. Tsirlin, N. Hollmann, Y.Y. Chin, H.-J. Lin, C.T. Chen, A. Tanaka, L.H. Tjeng, Z. Hu, Dalton Trans. 44 (2015) 10708–10713.
[39] E. Skoropata, T. T. Su, H. Ouyang, J. W. Freeland and J. van Lierop, Phys. Rev. B, DOI:https://doi.org/10.1103/PhysRevB.96.024447.
[40] H. Ikeno, J. Appl. Phys. 120 (2016) 142104.
[41] J. A. Moyer, C. A. F. Vaz, E. Negusse, D. A. Arena and V. E. Henrich, Phys. Rev. B, DOI:https://doi.org/10.1103/PhysRevB.83.035121.
[42] A. Lopez-Ortega, M. Estrader, G. Salazar-Alvarez, S. Estrade, I.V. Golosovsky, R. K. Dumas, D.J. Keavney, M. Vasilakaki, K.N. Trohidou, J. Sort, F. Peiro, S. Surinach, M.D. Baro, J. Nogues, Nanoscale 4 (2012) 5138.
[43] M. Estrader, A. López-Ortega, S. Estradé, I. V. Golosovsky, G. Salazar-Alvarez, M. Vasilakaki, K. N. Trohidou, M. Varela, D. C. Stanley, M. Sinko, M. J. Pechan, D. J. Keavney, F. Peiró, S. Suriñach, M. D. Baró and J. Nogués, Nat. Commun., DOI:https://doi.org/10.1038/ncomms3960.
[44] I.J. Bruvera, P. Mendoza Zélis, M. Pilar Calatayud, G.F. Goya, F.H. Sánchez, J. Appl. Phys. 118 (2015) 184304.
[45] D. Toulemon, B.P. Pichon, X. Cattoen, M.W.C. Man, Sylvie. Begin-Colin, Chem. Commun. 47 (2011) 11954–11956.
[46] J.A. De Toro, P.S. Normile, S.S. Lee, D. Salazar, J.L. Cheong, P. Muñiz, J.M. Riveiro, M. Hillenkamp, F. Tournus, A. Tamion, P. Nordblad, J. Phys. Chem. C 117 (2013) 10213–10219.
[47] S. Sasaki, K. Fujino, Y. Takéuchi, Proc. Jpn. Acad. Ser. B 55 (1979) 43–48.
[48] J. Nogues, I.K. Schuller, J. Magn. Magn. Mater. 192 (1999) 203.
[49] scar Iglesias, A. Labarta, Lcar, X. Batlle, J. Nanosci. Nanotechnol. 8 (2008) 2761.
[50] M. Pauly, B.P. Pichon, P. Panissod, S. Fleutot, P. Rodriguez, M. Drillon, Sylvie. Begin-Colin, J. Mater. Chem. 22 (2012) 6343–6350.
[51] W.H. Meiklejohn, C.P. Bean, Phys. Rev. 105 (1957) 904–913.
[52] Y. Suzuki, R.B. van Dover, E.M. Gyorgy, J.M. Phillips, R.J. Felder, Phys. Rev. B 53 (1996) 14016–14019.
[53] J. Nogues, V. Skumryev, J. Sort, S. Stoyanov, D. Givord, Phys. Rev. Lett. 97 (2006) 157203.
[54] M. Tadic, D. Nikolic, M. Panjan, G.R. Blake, J. Alloys Compd. 647 (2015) 1061–1068.